

Stability and Reactions of CaCO₃ polymorphs in the Earth's Deep Mantle

Zhigang Zhang^{1,2,3*}, Zhu Mao⁴, Xi Liu⁵, Yigang Zhang^{3,1,2,3} and John Brodholt⁷

¹ Key Laboratory of Earth and Planetary Physics, Institute of Geology and Geophysics, Chinese Academy of Sciences, Beijing, 100029, China.

² Institutions of Earth Science, Chinese Academy of Sciences, Beijing, 100029, China.

³ [College of Earth and Planetary Sciences](#), University of Chinese Academy of Sciences, Beijing 100049, China.

⁴ Laboratory of Seismology and Physics of Earth's Interior, School of Earth and Planetary Sciences, University of Science and Technology of China, Hefei, Anhui, China

⁵ Key Laboratory of Orogenic Belts and Crustal Evolution, MOE, Peking University, Beijing 100871, China

⁶ School of Earth and Space Sciences, Peking University, Beijing 100871, China

⁷ Department of Earth Sciences, University College London, Gower Street, London, WC1E 6BT, United Kingdom

* Corresponding author: Zhigang Zhang (zgzhang@mail.iggcas.ac.cn)

Key Points:

- The phase boundaries of CaCO₃ polymorphs are sensitive to temperature at high pressures.
- At high temperatures, the high pressure re-stabilization of CaCO₃ over MgCO₃ is found to be unfavorable.
- CaCO₃ polymorphs readily reacts with SiO₂ even in the cold subduction slabs down to the Earth's deep mantle.

1

2 **Abstract**

3 As an important component of carbonates in the mantle, CaCO_3 is a major carrier of
4 carbon from the surface to the deep interiors. In recent years, new varieties of CaCO_3
5 polymorphs have been continuously predicted by first principles simulations and verified by
6 experiments. The findings of these polymorphs open the possibility of stabilizing CaCO_3
7 component in the lower most mantle. Here, through extensive first principles simulations, we
8 inspect the stability and reactions of high-pressure CaCO_3 polymorphs at high temperatures.
9 ~~Special efforts were made to eliminate the systematic errors in the simulation results and increase~~
10 ~~the predictability of the simulations. Systematic errors from approximations to the exchange-~~
11 ~~correlation functional in density functional theory have been essentially eliminated with a~~
12 ~~generalized rescaling method to increase the predictability of the simulations.~~ We find
13 temperature has important effects on the stabilities and the reactions of CaCO_3 polymorphs with
14 mantle minerals. In particular, the tetrahedrally structured CaCO_3 -polymorph (space group
15 $P2_1/c$) is found to be sensitive to temperature with a positive Clapeyron slope of 15.81(6)
16 MPa/K. Reacting with MgSiO_3 , CaCO_3 is shown to be less stable than MgCO_3 over the whole
17 mantle pressures (to ~136 GPa) above ~1500 K. And CaCO_3 is demonstrated to readily react
18 with SiO_2 even in the cold subduction slabs. Thus high temperature greatly increases the
19 tendency of partitioning calcium into the silicates and CaCO_3 is not likely to be the major host of
20 carbon in the Earth's deep mantle.

21

22

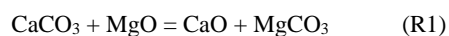
23 **1 Introduction**

24 CaCO_3 is a common component in rocks at the Earth's surface and in the marine
25 sediments. Through the transport of altered oceanic lithosphere and carbonaceous sediments in
26 subduction zones, it can be cycled into the mantle and may have impacts as far down to the
27 transition zone or lower mantle as inferred from inclusions in the sublithospheric minerals and
28 diamonds (Kaminsky, 2012; Zedgenizov et al., 2016). As a vital proxy of carbon (Keppler et al.,
29 2003; Luth, 1999), CaCO_3 is important not only in connecting the surficial volatiles with those in
30 the Earth's interiors (Luth, 1999;2014), but also in the melting in the mantle (Hammouda &
31 Keshav, 2015), and may be closely related with the formation of super-deep diamonds (Walter et
32 al., 2011). The phase relations of CaCO_3 and its reactions with other minerals are indispensable
33 to quantitatively understand the roles played by CaCO_3 in the deep mantle.

34 Through decades of experimental and theoretical efforts, current knowledge of phase
35 relations in carbonate systems advance significantly (see Shatskiy et al. (2015) and references
36 therein). For the end-member CaCO_3 , recent studies at high pressures demonstrate that it shows
37 more complex structures and has a greater variety of polymorphs than expected. Besides the
38 well-known calcite (and related metastable phases calcite I-III) and aragonite (Suito et al., 2001),
39 compressed polymorphs of CaCO_3 have been predicted by ab initio simulations (Oganov et al.,
40 2006; Oganov et al., 2008) and verified by high pressure experiments (Merlini et al., 2012; Ono
41 et al., 2007). Pickard and Needs (2015) carried out calculations using ab initio random structure
42 searching technique and discovered some additional monoclinic CaCO_3 -polymorphs that are
43 more stable at the pressures of the topmost and lower part of the lower mantle. Through state-of-

44 the-art *in-situ* experimental techniques, these new phases or their analogues have been observed
 45 in several most recent studies (Gavryushkin et al., 2017; Lobanov et al., 2017; Li et al., 2018).
 46 Despite the findings of these high-pressure polymorphs, there are still significant uncertainties as
 47 to the stability of CaCO₃-polymorphs at simultaneously high pressures and high temperatures
 48 and remarkable discrepancies still exist in the phase boundaries constrained from different
 49 approaches (Li et al., 2018).

50 The greater variety of CaCO₃-polymorphs as compared with other carbonate components
 51 increases the possibility that CaCO₃ may be stable at high pressures in the lower mantle (Oganov
 52 et al., 2008; Pickard & Needs, 2015). Considering the major minerals in the lower mantle and
 53 basaltic subduction slabs, three typical reactions are relevant (Oganov et al., 2008):



57 Previous theoretical calculations find that the reactants in reactions (R1) and (R3) are more stable
 58 relative to the products over the mantle pressures (Oganov et al., 2008; Pickard & Needs, 2015).
 59 They also show that the stability of CaCO₃ over MgCO₃ in reaction (R2) can be achieved above
 60 ~100 GPa (Pickard & Needs, 2015). Thus CaCO₃ could be re-stabilized and become the main
 61 host of carbon in the lower most mantle. This is opposed to extrapolations from experiments at
 62 modest pressures (Biellmann et al., 1993; Li et al., 2018). Since these **previous simulations have**
 63 **not considered the vibrations of ions were carried out under static conditions ($T=0$)**, it is unclear
 64 whether or not the predicted re-stabilization of CaCO₃ still hold at high temperatures.

65 To inspect the stability and reactions of CaCO₃ polymorphs in the Earth's deep mantle,
 66 especially at high temperatures, we systematically investigated the phase boundaries of the
 67 CaCO₃ and the reaction lines of (R1-R3) over mantle *T-P* conditions in this study. Extensive first
 68 principles lattice dynamics and molecular dynamics simulations have been carried out to
 69 comprehensively clarify the temperature effects. Our calculations in this study demonstrate that
 70 CaCO₃ readily reacts with silicates even along the temperature profiles in cold subduction slabs
 71 and therefore cannot be the major host of carbon in the deep mantle.

72

73 2 Methods

74 2.1. Candidate phases and nomenclatures

75 Based on previous theoretical studies (Oganov et al., 2006; Oganov et al., 2008; Pickard
 76 & Needs, 2015) and experiments (Merlini et al., 2012; Ono et al., 2007; Ono et al., 2005), we
 77 consider eight high pressure polymorphs of CaCO₃ that are relevant to the mantle conditions in
 78 this study, namely: aragonite (space group *Pmnc*), “aragonite-II” (space group *P2₁/c*), “post-
 79 aragonite” (space group *Pmmn*), “CaCO₃-*P2₁/c-l*”, “CaCO₃-*Pnma-h*”, “CaCO₃-*P2₁/c-h*”,
 80 “pyroxene-type” (space group *C222₁*) and “CaCO₃-VI” (space group *P1̄*). Since most of these
 81 polymorphs have no official names yet, we use the same nomenclatures (non-officials with
 82 quotation marks) as in the previous studies for better references. In particular, the “aragonite-II”
 83 phase is a distorted structure of aragonite proposed by Gavryushkin et al. (2017); the “post-
 84 aragonite” phase corresponds to that examined in the experiments by Ono et al. (2005) and

带格式的: 字体: 倾斜

85 simulations by Oganov et al. (2006); the phases of “CaCO₃-P2₁/c-I”, “CaCO₃-Pnma-h” and
86 “CaCO₃-P2₁/c-h” are those predicted by Pickard and Needs (2015), among which the “CaCO₃-
87 P2₁/c-I” phase is similar to the “CaCO₃-VII” phase observed by Gavryushkin et al. (2017) and Li
88 et al. (2018) and the “CaCO₃-P2₁/c-h” phase is closely related with that detected by Lobanov et
89 al. (2017); the “pyroxene-type” phase corresponds to the “phase I” predicted by Oganov et al.
90 (2006) and may be relevant to that found by Ono et al. (2007); and finally the “CaCO₃-VI” phase
91 as found by Merlini et al. (2012), is similar to the “phase II” predicted by Oganov et al. (2006).
92 For convenience all these structures are provided in the supporting information (Data Set S1) in
93 the form of crystallographic information files (.cif).

94

95 2.2. Simulations

96 First principles simulations are carried out with VASP with the projector-augmented-
97 wave (PAW) method (Kresse and Joubert, 1999). We focus on the Local Density Approximation
98 (LDA) in this study, and eliminate the systematic errors through the well-established re-scaling
99 method proposed in our previous studies (Zhang and Liu, 2015; Zhang et al., 2013). The core
100 radii are 2.3 a.u. for Ca (with [Ne] core), 1.5 a.u. for C (with [He] core), 1.52 a.u. for O (with
101 [He] core).

102 Lattice constants and internal coordinates in the unit cells of the CaCO₃ polymorphs at
103 static conditions are fully relaxed with an energy cutoff of 1000 eV for the plane wave basis set
104 and a convergence criterion of 10⁻⁸ eV for the electronic self-consistent loop. We use a Brillouin
105 zone sampling grid of spacing 0.3 Å⁻¹, which is well converged as revealed by our benchmarks
106 with finer spacing of 0.2 Å⁻¹.

107 Lattice dynamics (LD) simulations are carried out through finite displacement method
108 with the aid of the package Phonopy (Togo and Tanaka, 2015). The interatomic force constants
109 are calculated by setting a displacement amplitude of 0.01 Å for each atom. The supercell is
110 defined with the length of each lattice vector larger than 8 Å and therefore contains 80-160 atoms
111 ([details of the constructed supercells and number of atoms for the eight polymorphs are listed in](#)
112 [the supporting information \(Table S1\)](#)). To evaluate the vibrational density of state (VDOS), a
113 32×32×32 mesh is used for the *q*-point sampling in the first Brillouin zone. In the framework of
114 quasi-harmonic approximation theory, we can conveniently obtain various thermodynamic
115 properties at finite temperatures through options provided by Phonopy. The generated parameters
116 for the Birch-Murnaghan equation of state (EOS) from 300 K to 900 K can be found in Data Set
117 S2 in the supporting information.

118 We have also carried out extensive molecular dynamics (MD) simulations from 1000 K
119 to 3500 K to account for possible anharmonicity that may be important at high temperatures
120 ([Zhang et al., 2013](#)). The equivalent supercells used in the above-mentioned phonon calculations
121 are constructed for the MD simulations. At each time step (1 fs interval), the electronic structure
122 is calculated at the Brillouin zone center with an energy cutoff of 500 eV and iteration
123 convergence criterion of 10⁻⁶ eV. MD trajectories are propagated in the *NVT* ensemble with the
124 Nosé thermostat for 5-10 ps, with the first 3 ps discarded for pre-equilibrium. [Larger supercells](#)
125 [and longer durations generate unchanged properties within the statistical uncertainties](#). We
126 carefully inspect the simulated structures in the MD trajectories to ensure that the correct phase

127 is maintained during the calculations of the thermodynamic properties. These MD simulation
128 results are regressed with the following Mie-Gruneisen EOS:

$$129 \quad P(V, T) = P_c(V, T_s) + \frac{\gamma}{V} C_V (T - T_s) \quad (1)$$

130 where P_c is the reference isotherm at $T_s=900$ K (also serve as the switching temperature as
131 mentioned in section 3.1) that can be accurately reproduced with the Birch-Murnaghan EOS, γ is
132 the Gruneisen parameter and we simplify it to be linear with V by $\gamma = \gamma_a + \gamma_b^*(V - V_{s0})/V_x$ (V_{s0} is the
133 volume at zero pressure and T_s ; V_x is an arbitrary auxiliary parameter, which is chose here to be
134 $40.1873 \text{ cm}^3/\text{mol}$ as consistent with our previous study (Zhang & Liu, 2015)), C_V is the isochoric
135 heat capacity. Keeping the parameters at T_s the same as those by LD simulations, we regress the
136 ~~simulated~~ pressures and internal energies differences respect to those at T_s and get the parameters
137 as listed in Table S4~~2~~ in the supporting information.

138

139 2.3. Correction to the simulation results

140 It is well-known that LDA typically over-binds structures and therefore usually
141 underestimates the volumes in a wide variety of systems. As discussed in our previous studies
142 (Zhang and Liu, 2015; Zhang et al., 2013), the a posteriori generalized rescaling method can be
143 used to effectively eliminate the well-known systematic errors in the simulated volumes obtained
144 from density functional theory (DFT). The rescaling provides results that are essentially
145 independent of the choice of exchange-correlation functional, and is needed for obtaining
146 experimentally accurate results. If we choose the aragonite phase as a reference phase and 300 K
147 as a reference temperature ($T_0=300$ K), and by assuming the systematic errors depend only on the
148 volume and are the same for all phases, we get the following relationships for the Helmholtz free
149 energy and pressure:

$$150 \quad F(V, T) = F^{\text{LDA}}(V, T) - F_{\text{arag}}^{\text{LDA}}(V, T_0) + F_{\text{arag}}(V, T_0) \quad (2)$$

$$151 \quad P(V, T) = P^{\text{LDA}}(V, T) - P_{\text{arag}}^{\text{LDA}}(V, T_0) + P_{\text{arag}}(V, T_0) \quad (3)$$

152 The left hand side is the corrected value for the phase of interest at P and T , and the first
153 term on the right-hand side is the calculated value for the same phase at the same P and T . The
154 next two terms make up the correction to the LDA results based on the calculated (LDA) and
155 expected properties of aragonite respectively. The expected results of F_{arag} and P_{arag} at T_0 can be
156 further evaluated by rescaling the corresponding simulated results:

$$157 \quad F_{\text{arag}}(V, T_0) = F_{\text{arag}}(V_0^{\text{exp}}, T_0) + \frac{V_0^{\text{exp}} K_0^{\text{exp}}}{V_0^{\text{LDA}} K_0^{\text{LDA}}} \left[F_{\text{arag}}^{\text{LDA}} \left(V \frac{V_0^{\text{LDA}}}{V_0^{\text{exp}}}, T_0 \right) - F_{\text{arag}}^{\text{LDA}}(V_0^{\text{LDA}}, T_0) \right] \quad (4)$$

$$158 \quad P_{\text{arag}}(V, T_0) = \frac{K_0^{\text{exp}}}{K_0^{\text{LDA}}} P_{\text{arag}}^{\text{LDA}} \left(V \frac{V_0^{\text{LDA}}}{V_0^{\text{exp}}}, T_0 \right) \quad (5)$$

带格式的: 字体: 倾斜

带格式的: 下标

159 where subscript 0 refer to properties of aragonite at zero pressure and 300 K, and K is the
 160 isothermal bulk modulus. Note that in Eqn. (4) there is still an unknown parameter of
 161 $F_{\text{arag}}(V_0^{\text{exp}}, T_0)$ for deriving the absolute free energy. For the calculations of a one-component
 162 phase diagram, as presented in the next section, only the relative magnitude of the free energy is
 163 needed so that we can arbitrarily choose it to be $F_{\text{arag}}^{\text{LDA}}(V_0^{\text{LDA}}, T_0)$. The choices of other parameters
 164 in these formulas are described in the caption of Fig. 1.

165

166 3 Results and Discussion

167 3.1. Phase diagram of CaCO_3

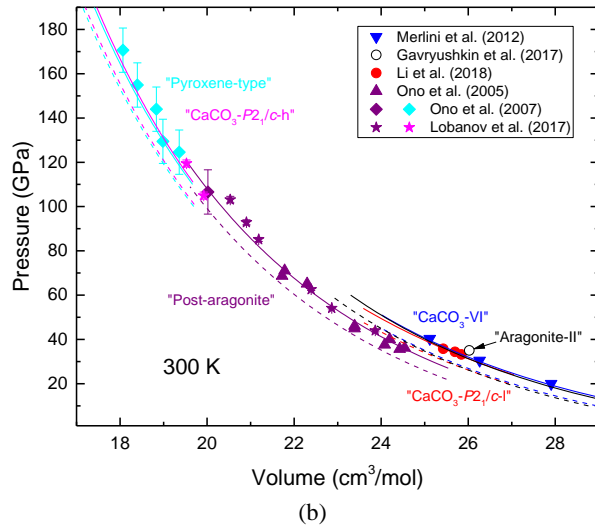
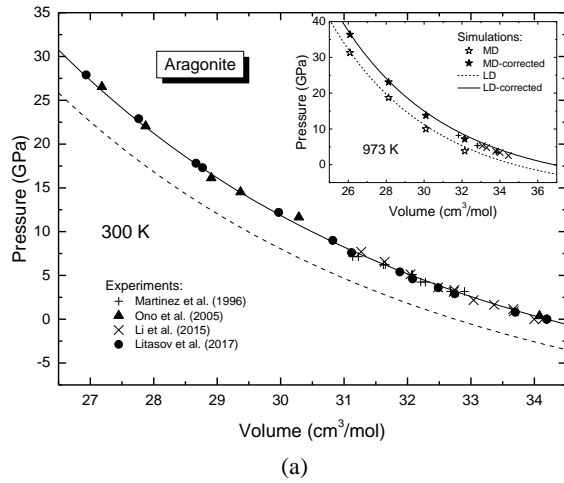
168 Many experimental measurements have been accumulated for aragonite, which facilitates
 169 a comparison with our simulations. We show in Fig. 1(a) that the simulations with the LDA
 170 underestimate the pressures by about 3-5 GPa over the T - P regime involved in the presently
 171 available experiments for aragonite. These volume-dependent systematic errors can be
 172 essentially eliminated through our above-mentioned re-scaling corrections, even for higher-
 173 temperature conditions (as revealed in the inset plot of Fig. 1(a)) and for other higher-pressure
 174 polymorphs (as shown in Fig. 1(b)). The success for the achieved accuracies in high pressure
 175 polymorphs is remarkable and important since most other polymorphs considered in this study
 176 have few or even no experimental data, especially at very high temperatures and pressures.

177 With a closer inspection over the high temperature data of the corrected results in the
 178 inset plot of Fig. 1(a), it can be found that the lattice dynamics (LD) simulations predict slightly
 179 higher pressures at large volumes while those simulated by molecular dynamics (MD) are in very
 180 good agreement with the experiments; this implies an increasingly prominent influence of
 181 anharmonicity. To combine the merits of both approaches, we choose a switching temperature
 182 (T_s) of 900 K, below which we adopt the LD simulation results to accurately account for the
 183 quantum effects and above which we use ~~these the thermal properties respect to T_s~~ by MD
 184 simulations to implicitly account for the possible anharmonicity. While it is possible to adopt
 185 more rigorous calculations for the anharmonicity at high temperatures (i.e. Monserrat, et al,
 186 2013; Zhang, et al., 2014), the simple way of combining the lattice dynamics and molecular
 187 dynamics simulations would be adequate for the purpose of this study.

188

带格式的: 字体: 倾斜

带格式的: 下标



189
190

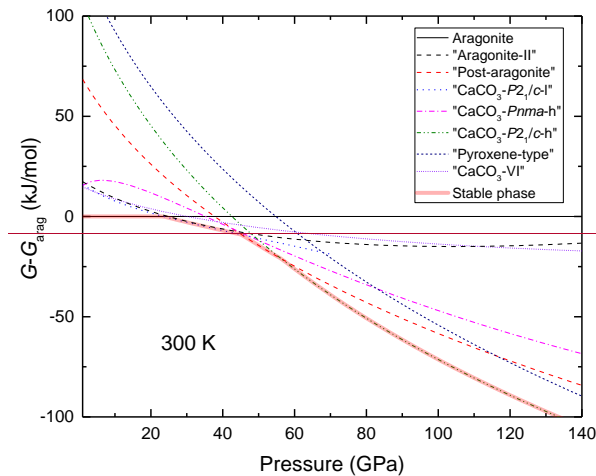
191
192

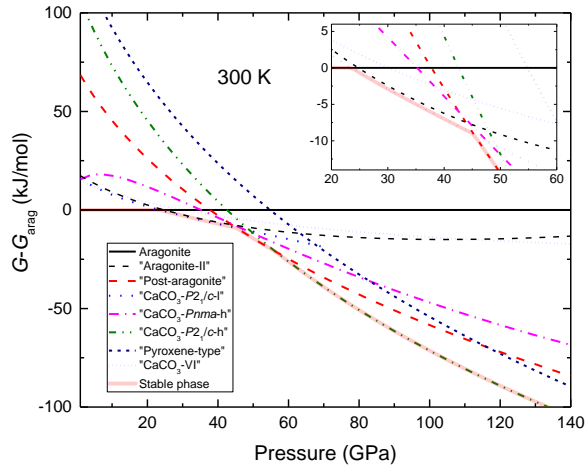
193 **Figure 1.** Comparisons between the simulations in this study and the experiments in the
 194 literature: (a) aragonite at 300 K and 973 K (inset); (b) other polymorphs at 300 K. The dashed
 195 curves and open stars (at 973 K) are the raw results by lattice dynamics (LD) simulations and
 196 molecular dynamics (MD) simulations, respectively. We apply the rescaling corrections to these
 197 raw results and obtain the solid curves and filled stars. The parameters for the re-scaling (Eqns.
 198 (2-5)) are: $V_0^{exp}=34.20 \text{ cm}^3/\text{mol}$ and $K_0^{exp}=67.1 \text{ GPa}$ (from Ono et al. (2005)); $V_0^{LDA}=32.75$
 199 cm^3/mol and $K_0^{LDA}=75.0 \text{ GPa}$. In (b), we plot the data (experiments with points and simulations
 200 with lines) for polymorphs in different colors: “CaCO₃-VI” in blue, “aragonite-II” in black,
 201 “CaCO₃-P₂/c-l” in red, “post-aragonite” in purple and “pyroxene-type” in cyan. Data for the

202 “CaCO₃-P2₁/c-h” phase, which is closely similar with the “pyroxene-type” phase, are also shown
 203 in magenta. Note that the pressures of the experiments by Ono et al. (2005; 2007) are re-
 204 calculated with a more accurate pressure-scale proposed by Fei et al. (2007).

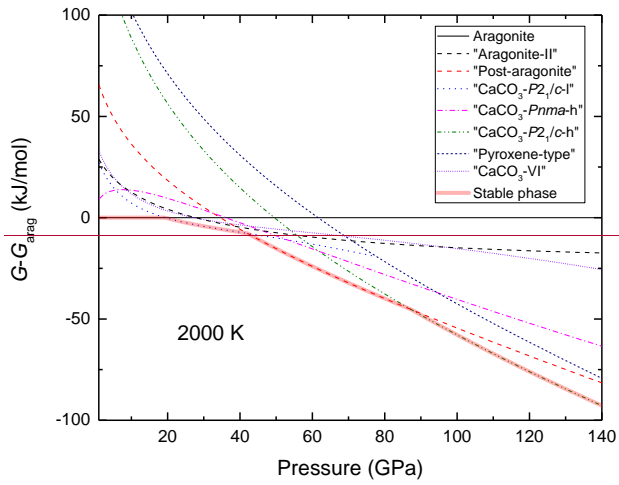
205
 206 The relative stabilities of the polymorphs considered in this study were evaluated from
 207 their Gibbs free energies. Applying the corrections to the systematic errors, we obtain the free
 208 energy curves relative to that of aragonite, as shown in Fig. 2. At 300 K, aragonite transforms to
 209 the “CaCO₃-P2₁/c-I” phase at 23.6 GPa and then to the “post-aragonite” phase at 45.2 GPa.
 210 When pressure is further increased to 56.4 GPa, the “CaCO₃-P2₁/c-h” phase becomes stable and
 211 persists to higher pressures. Increasing temperature to 2000 K slightly lowers the pressure of
 212 the first two phase transitions to about 19.4 GPa and 42.1 GPa but significantly broadens the phase
 213 regime of the “post-aragonite” phase to 87.4 GPa. The other four phases are unstable over the
 214 pressure and temperature range considered in this study. Among them, the “aragonite-II” phase
 215 is only marginally unstable relative to the stable phase with a minimum free energy difference of
 216 only about 0.4 kJ/mol (i.e. 0.8 meV/atom) in the vicinity of 30-40 GPa at 300 K. It should be
 217 noted that Gavryushkin et al. (2017) find the stability of “aragonite-II” phase in similar pressure
 218 range at 0 K. The apparent discrepancy can be ascribed to the different simulation details and
 219 also such small energetic differences. At 2000 K, the energy difference increases to larger than
 220 2.5 kJ/mol (i.e. 5 meV/atom), which means the “aragonite-II” phase becomes increasingly
 221 unstable at high temperatures. The “CaCO₃-Pnma-h” phase similarly approaches quite near the
 222 stable phase right around the phase transition from the “CaCO₃-P2₁/c-I” phase to the “post-
 223 aragonite” phase with minimum free energy differences of about 1.0 and 4.0 kJ/mol at 300 K and
 224 2000 K, respectively. The “CaCO₃-VI” phase also approaches the stable phase at around 24 GPa,
 225 where the aragonite begins to be unstable, with minimum free energy differences of about 2.4
 226 and 3.3 kJ/mol at these two temperatures. The “pyroxene-type” phase, which resembles the
 227 “CaCO₃-P2₁/c-h” phase with fourfold coordinated carbon atoms, seems to be quite unstable with
 228 a free energy significantly higher than that of the stable phases by over 13.5 kJ/mol.

229





(a)

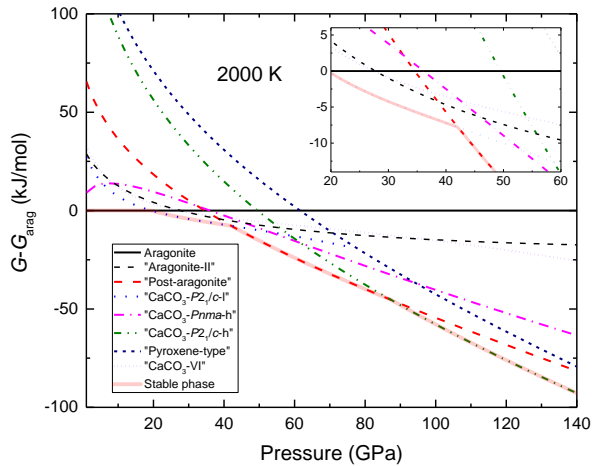


域代码已更改

带格式的: 左, 缩进: 左侧: 0 厘米, 首行缩进: 0 字符

231
232
233

234



(b)

235

236

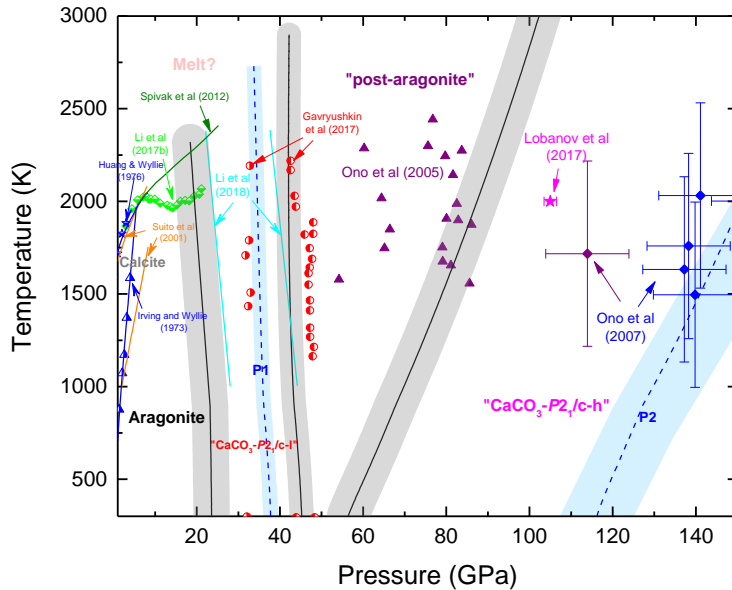
237 **Figure 2.** Gibbs free energies of CaCO_3 polymorphs relative to that of aragonite at (a) 300 K and
 238 (b) 2000 K. The thermodynamic stable phase with the lowest Gibbs free energy is marked with
 239 shaded red line. Insets are the focused plots within the pressure regime of 20-60 GPa to show the
 240 small free energy differences more clearly.

241

242 By connecting the intersections of the free energy curves, we obtain the phase diagram of
 243 CaCO_3 in Fig. 3. The transition pressures between the phase “ $\text{CaCO}_3\text{-}P2_1/c\text{-}l$ ” and its
 244 neighborhoods (aragonite at the lower pressure side and “post-aragonite” at the higher pressure
 245 side) are relatively insensitive to temperature. The Clapeyron slopes of the boundaries are
 246 slightly negative and are around $-1.97(4)$ MPa/K, which is quite close to the most recent
 247 experimental measurements (Li et al., 2017a). The upper phase boundary of the “post-aragonite”
 248 phase, on the other hand, is very sensitive to temperature, with an average Clapeyron slope of
 249 $15.81(6)$ MPa/K. Compared with the transition slopes, the absolute positions of the phase
 250 boundaries have more uncertainty since the free energy differences between the adjacent phases
 251 are small around the transition points. We have evaluated the uncertainties of the phase
 252 boundaries by considering a typical ~~cumulative~~ error of 2 kJ/mol in the calculated free energy
 253 contrast of the coexisting phases. As shown in Fig. 3, within the uncertainties, the predicted
 254 phase regions agree quite well with those experimentally-determined for the “post-aragonite”
 255 phase (Ono et al., 2005). For the “ $\text{CaCO}_3\text{-}P2_1/c\text{-}l$ ” phase, its upper boundary is predicted in good
 256 agreement with recent experiments (Gavryushkin et al 2017; Li et al., 2018), while its lower
 257 boundary is slightly lower than that determined by Li et al (2018) and remarkably lower than that
 258 observed by Gavryushkin et al (2017). The recent experimental observation of the “ $\text{CaCO}_3\text{-}$
 259 $P2_1/c\text{-}h$ ” phase (Lobanov et al., 2017) lies right at the predicted phase regime in this study while
 260 the onset of the transition pressure (~ 103 GPa at ~ 2000 K) is higher than the predicted boundary
 261 here ($\sim 87.4 \pm 6.6$ GPa).

域代码已更改

262



263

264 **Figure 3.** Phase diagram of CaCO₃ based on previous experimental measurements and current
 265 first principles simulations. The three black solid curves are the predicted phase boundaries of
 266 the stable polymorphs as indicated with bold colored texts. The blue dashed curves are the
 267 predicted pseudo phase boundary between the aragonite and “post-aragonite” (marked as P1) and
 268 that between the “post-aragonite” and “pyroxene-type” phases (marked as P2), as discussed in
 269 section 3.2. The shadows around these curves show the effects of uncertainties in the free energy
 270 (illustrated with a typical 2 kJ/mol here) on the predicted phase boundaries. For the experimental
 271 data, the half-filled symbols are on the phase boundaries while the filled symbols are in the one-
 272 phase field (in purple for “post-aragonite”, in magenta for “CaCO₃-P₂₁/c-h” and in blue for
 273 “pyroxene-type”, in red for “CaCO₃-P₂₁/c-l”). The olive curve is the melting curve determined
 274 by Spivak et al (2012). The cyan straight lines are the phase boundaries for the “CaCO₃-P₂₁/c-l”
 275 as estimated by Li et al. (2018).

276

277 3.2. Kinetic effects for the stability of CaCO₃

278 Compared with silicates, carbonates show much complexity with more varieties of
 279 reversible metastable transitions, which introduces challenges for experimental measurements
 280 and theoretical predictions. Through our calculations in this study, we have found that the free
 281 energy differences among adjacent polymorphs are very small. As mentioned above, the
 282 “CaCO₃-VI” phase excluded from the phase diagram in Fig. 3 is actually only slightly unstable
 283 relative to the stable phases (Fig. 2). Therefore, its presence in high pressure experiment from
 284 ~15 GPa to ~40 GPa (Merlini et al., 2012) may be explained either by possible uncertainties in

our calculations or by kinetic barriers of equilibrium phase transitions often encountered in the experiments (Ono et al., 2005; Ono et al., 2007). The observations of the “aragonite-II” phase in the recent experiment by Gavryushkin et al. (2017) can be explained in the same manner.

Another noticeable deviation of our calculated phase diagram from the experiments is that the predicted stable phase at highest pressures (to over 140 GPa) is not in accordance with the experimentally-observed one by Ono et al. (2007). As pointed out by Pickard and Needs (2015), the limited resolution of the experimental spectrum at these extreme pressures may not allow a good discrimination between the “pyroxene-type” phase claimed by Ono et al (2007) and the energetically much more stable “CaCO₃-P_{21/c-h}” phase. Alternatively, it is possible that the discrepancy may be ascribed to the energy barriers along the possible phase transition routes taken by the experiments. Although quantitative evaluations of the kinetic reaction barriers are out of the scope of this study, the compression of CaCO₃ seems to follow two different phase transition routes with high barriers in between: one is the “orthorhombic phase transition route” from aragonite to “post-aragonite” and finally to the “pyroxene-type” phase, while the other is the “monoclinic phase transition route” from the “CaCO₃-P_{21/c-l}” phase to the “CaCO₃-P_{21/c-h}” phase. The energy barriers for the phase transitions along either of these routes are likely to be small as compared to those for the phase transitions between the two routes. Indeed, the “CaCO₃-P_{21/c-l}” phase is found to spontaneously collapse to the “CaCO₃-P_{21/c-h}” phase at around 70-80 GPa without any energy barrier. And the recent study of Lobanov et al. (2017) proved that the barrier height between “post-aragonite” and “CaCO₃-P_{21/c-h}” is large. In this sense it seems to be plausible that two additional metastable phase transition boundaries may be more relevant to the experiments interfered by the kinetic barrier problem in this pressure range. In Fig. 3, the blue dashed line marked with “P1” is for the transition from the aragonite to “post-aragonite”, and that marked with “P2” is for the transition from the “post-aragonite” to “pyroxene-type” phase. The Clappayon slopes of these two phase transitions are similar to those of the phase transitions “CaCO₃-P_{21/c-l}”-“post-aragonite” and “post-aragonite”-“CaCO₃-P_{21/c-h}”. Within the uncertainties, the experimental findings by Ono et al. (2007) can be reasonably explained in this way.

313

3.3. Reactions (R1) and (R2)

In these two reactions, five polymorphs of MgCO₃ have been included in our extensive molecular dynamics and lattice dynamics simulations, namely, conventional magnesite (space group $R\bar{3}c$), “MgCO₃-phase II” (space group $C2/m$) and “MgCO₃-phase III” (space group $P2_1$) as predicted by Oganov et al. (2008), “MgCO₃-P $\bar{1}$ ” and “MgCO₃-P₂₁₂₁₂₁” as predicted by Pickard and Needs (2015). These structures are also included in the supporting information (Data Set S1). Using the same approach as for CaCO₃ described above, we obtain a phase diagram for MgCO₃ composition as shown in Fig. 4. The “MgCO₃-phase III” and “MgCO₃-P₂₁₂₁₂₁” are found to be closely equivalent in energy and are stable above ~144 GPa. Therefore, in the inner plot of Fig. 4 only three polymorphs are involved and the “MgCO₃-P $\bar{1}$ ” phase finds its stability in a limited regime, which explains the recent experiments that magnesite transforms directly to “MgCO₃-phase II” at high temperatures (Maeda et al., 2017).

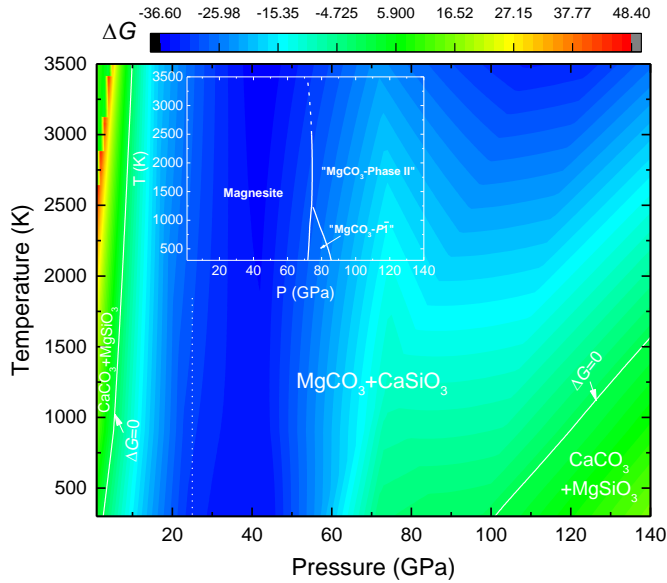
For the silicates and oxides in these two reactions, we calculated their free energies in the framework of quasi-harmonic approximation theory by considering the following polymorphs:

328 MgSiO₃ in bridgmanite and “post-perovskite” structures (Oganov and Ono, 2004; Zhang et al.,
329 2013); CaSiO₃ in tetragonal perovskite *I4/mcm* structure (Stixrude et al., 2007) ; MgO in rocksalt
330 structure; CaO in B1 (NaCl) and B2 (CsCl) structures. The core radii 2.3 a.u. for Ca (with [Ne]
331 core), 2.0 a.u. for Mg (valence configuration with p semi-core valence state, 2p⁶3s²), 1.5 a.u. for
332 C (with [He] core), 1.6 a.u. for Si (with [Ne] core), 1.52 a.u. for O (with [He] core). The
333 supercells and number of atoms for these phases are listed in the supporting information (Table
334 S1). The other simulation settings for MgCO₃, MgSiO₃, CaSiO₃, MgO, CaO and SiO₂ are
335 essentially identical with those for CaCO₃, with LDA and PAW implementation of VASP and
336 also with the aid of Phonopy.

337 All the simulated properties of reactants and products in these reactions are corrected
338 using the rescaling method, with the reference free energies at standard condition ($F(V_0^{\text{exp}}, T_0)$ in
339 Eqn. 4) selected from the self-consistent thermodynamic database compiled by Holland et al.
340 (2013). The rescaling parameters for all the relevant compositions can be found in the supporting
341 information (Table S3). From the derived ΔG (free energy change) of the reaction (R1), we find
342 the CaCO₃ + MgO are much more stable than CaO + MgCO₃ over the temperature and pressure
343 ranges interested in this study, which means the athermal stability of the reactants as predicted by
344 Oganov et al. (2008) and Pickard and Needs (2015) still hold at high temperatures. The ΔG of
345 reaction (R2), on the other hand, shows more complex variations as revealed in Fig. 4.

346 It is clear from Fig. 4 that the products of the reaction (R2) are significantly more stable
347 than the reactants from ~20 GPa to ~50 GPa, which is in agreement with previous experimental
348 observations over similar pressure range (Biellmann et al., 1993). At lower pressures, the trend
349 shown in Fig. 4 agrees with the experimental findings of more calcic carbonates with decreasing
350 pressure (Luth, 1999), although this may only be regarded as illustrative since the bridgmanite
351 and CaSiO₃-perovskite we considered in our calculations are only stable above ~25 GPa in the
352 mantle (vertical dotted line). At higher pressures, the higher density of the CaCO₃-polymorph
353 relative to the MgCO₃-polymorph greatly diminishes the free energy change of reaction (R2),
354 especially at pressures above ~70 GPa at low temperatures. The CaCO₃ would be finally
355 stabilized relative to the MgCO₃ at ~100 GPa at 300 K, which agrees with the calculations by
356 Pickard and Needs (2015). On the other hand, the pressure-induced re-stabilization of CaCO₃ is
357 found to be hindered by the entropic effects of temperature and the field of MgCO₃ + CaSiO₃
358 opens towards higher pressures with increasing temperature. If we further take into account the
359 phase transformation and noticeable anharmonicity of CaSiO₃-perovskite (as compared with
360 MgSiO₃ polymorphs) (Stixrude et al., 2007), the stability region of MgCO₃ in reaction (R2)
361 would be even more expanded.

362



363
 364 **Figure 4.** Relative stability of CaCO₃ and MgCO₃ from the Gibbs free energy change (ΔG) of
 365 reaction (R2). Phase relations of MgCO₃ polymorphs up to 140 GPa and 3500 K are shown in
 366 the inset plot. The vertical dotted line corresponds to ~25 GPa above which bridgmanite and
 367 CaCO₃-perovskite become stable.

368
 369

370 3.4. Reaction (R3)

371 As shown in Fig. 5 with the bold solid line, the reaction line of (R3) has already been
 372 tightly constrained up to over 50 GPa in our recent measurements with synchrotron X-ray
 373 diffraction in laser-heated diamond anvil cells (Li., et al., 2018). To extend this line to even
 374 higher pressures without the need of modeling CO₂ and O₂, which are still inadequate and
 375 challenging (Litasov, et al., 2011a; Litasov, et al., 2017), we find the following reaction
 376 examined Reaction (R3) is more complex than the two mineral reactions mentioned above since
 377 the volatile phases of CO₂ or O₂ may be fluids, whose free energies are much more challenging
 378 to be computed. Getting around this problem, we propose an indirect way to constrain the
 379 reaction line for (R3) with our results mentioned above and the most recent experimental data.
 380 As shown in Fig. 5, the following reaction has been experimentally determined by Maeda et al.
 381 (2017)



383 which is can be closely related to reaction (R3) by

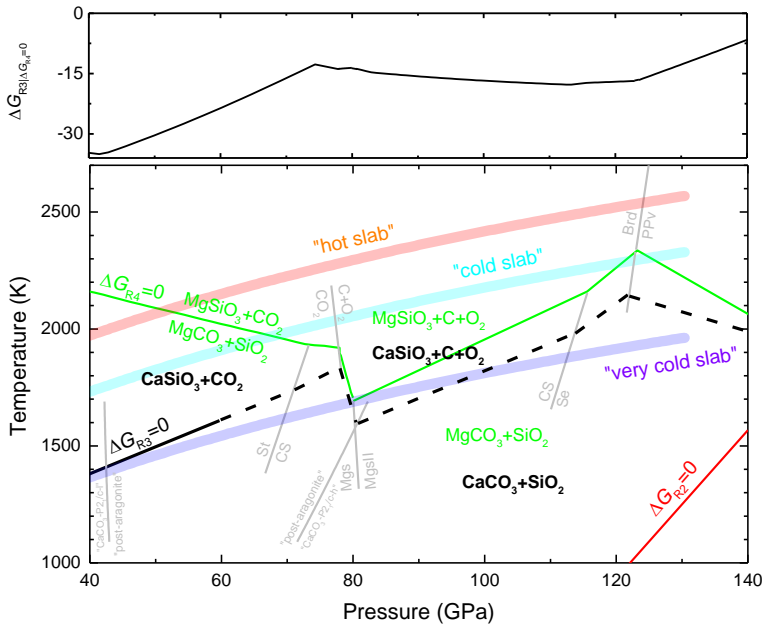
$$384 \Delta G_{R3} = \Delta G_{R2} + \Delta G_{R4} \quad (7)$$

带格式的: 下标

带格式的: 下标

385 Since $\Delta G_{R2} < 0$ over the mantle conditions as mentioned above, it can be inferred that the
 386 reaction line of (R3) should lie below (i.e., at lower temperature than) that of (R4), which is in
 387 accord with our recent measurements (Li et al., 2018). If we calculate the ΔG of reaction (R3)
 388 along the reaction line of (R4) (denoted as $\Delta G_{R3/\Delta G_{R4}=0}$), which equals ΔG_{R2} according to Eqn. (7)
 389 since $\Delta G_{R4}=0$, we find it approximately varies in three stages: first increases quickly from ~40
 390 GPa to ~75 GPa, then slightly decreases to ~120 GPa, and then further increases and finally
 391 approaches zero, as shown at the top of Fig. 6. Assuming ΔG would be in proportion to the
 392 temperature (since the entropic difference (ΔS) of the reactions are relatively insensitive to the
 393 pressure), the opposite trends between the slopes of the two reactions (R3) and (R4) at relatively
 394 lower pressures can be plausibly explained by the initial increase of $\Delta G_{R3/\Delta G_{R4}=0}$. Then the slight
 395 decrease of $\Delta G_{R3/\Delta G_{R4}=0}$ in the second stage may result in a slightly departing but almost parallel
 396 extension of both reaction lines. The further increase in the third stage would gradually lead to an
 397 intersection point where the three reactions meet. With these constraints and considering the
 398 possible phase transformations of each component, we finally obtain the reaction line of (R3) as
 399 shown in Fig. 5 (Maeda et al., 2017).

400



401

402 **Figure 5.** Schematic reaction line of (R3) based on the recent experimental constraints and
 403 simulated data in this study. The phase diagram of the $MgCO_3$ - SiO_2 system, with measured
 404 reaction line of (R4) (in green) and phase boundaries of relevant phases (St: stishovite; CS:
 405 $CaCl_2$ -type SiO_2 ; Se: seifertite; Mgs: magnesite; MgsII: magnesite-phase II; Brd: bridgmanite;

406 PPv: MgSiO₃-post-perovskite), follows that proposed by Maeda et al. (2017). Phase boundaries
407 of CaCO₃ polymorphs predicted in this study are included with light-gray solid lines. The
408 reaction line of (R3) below 60 GPa (in bold solid line) is the measured curve in our recent study
409 (Li et al., 2018) and that above 60 GPa (in bold dashed line) is extended by considering the phase
410 boundaries and the free energy change of reaction (R3) (ΔG_{R3}) along the reaction line of (R4)
411 ($\Delta G_{R4}=0$), as plotted on the top of the figure. The reaction line of (R2) ($\Delta G_{R2}=0$) is shown in red.
412 Geotherms of subducted slabs are shown after Maeda et al. (2017).

413
414 It should be noted that this indirect way of extending the reaction line of (R3) may
415 involve noticeable uncertainty, mostly from that of the reaction line of (R4). Although Maeda et
416 al. (2017) constrains the de-carbonation reaction boundaries of MgCO₃ much more precisely
417 with increased number of high *T-P* measurements as compared with its previous studies (e.g.,
418 Seto, et al., (2008)), the temperature and pressure uncertainties for each data point are still
419 remarkable (up to 10 GPa and 370 K, see Fig. 2 and Table S1 in Maeda et al. (2017)). The steep
420 gradient of decomposition boundary of CO₂ as shown in Fig. 5, in particular, should be highly
421 uncertain and is apparently inconsistent with the previous estimations (Litasov, et al., 2011a). On
422 the other hand, since we have precise estimations of the reaction boundary up to ~60 GPa, and
423 the decomposition slope of CO₂ seems to be negative (see Fig. 4 in Litasov et al. (2011a)), the
424 higher pressure extension would not significantly deviate from that depicted in Fig. 5.

425

426 3.5. Implications for the fate of CaCO₃ in the deep mantle

427 From the new constraints obtained in this study and taking into account the solidi of
428 carbonate systems (Litasov et al., 2013; Thomson et al., 2014) as shown in the integrated
429 diagram in Fig. 6, we may obtain a clearer picture on the fate of CaCO₃ in the deep mantle:

430 Firstly, a large proportion of CaCO₃ component would be transported and melted along
431 with the other carbonate components in many slabs up to the top region of the lower mantle (~20
432 GPa, rarely to ~50 GPa, as enclosed by the solidi of the CaCO₃-MgCO₃ system and alkaline
433 carbonate). As noticed by Litasov (2011b) and Kakizawa et al (2015), eutectic melting of CaCO₃
434 and MgCO₃ with silicates in the pressure range of 6-30 GPa may also take effects. Rapidly
435 percolating through the surrounding mantle and moving upwards due to their buoyancy
436 (Hammouda & Laporte, 2000), the generated calcic carbonatite melts are closely related with the
437 formation of diamond (Rohrbach & Schmidt, 2011; Hammouda & Keshav, 2015).

438 Secondly, a few CaCO₃ component survived from melting in the cold slabs would readily
439 react with MgSiO₃ and SiO₂. Due to the temperature effects, calcium prefers to be partitioned
440 into the silicates as CaSiO₃ (e.g., through reactions R2 and R3). Different from redox melting
441 and freezing (Rohrbach & Schmidt, 2011), these reactions of CaCO₃ provide alternative route to
442 produce deep diamonds or deep volatiles of CO₂ or O₂.

443 Thirdly, when CaCO₃ is transported in the “very cold” slabs with very low temperatures,
444 the free energy changes of reactions (R2) and (R3) are small. Taking into account the sluggish
445 kinetics in solid phases, the possibility of CaCO₃-bearing solid solutions with other carbonate
446 components in these slabs cannot be fully excluded.

447

带格式的: 缩进: 首行缩进: 1.27 厘米

带格式的: 下标

带格式的: 字体: 倾斜

带格式的: 字体: 倾斜

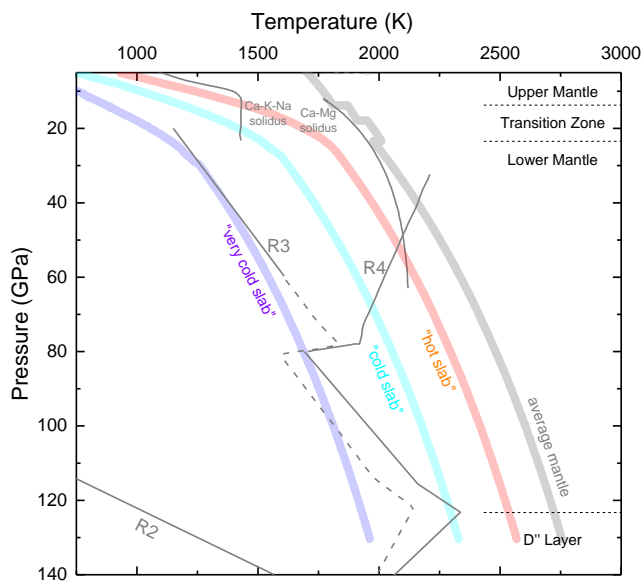
带格式的: 下标

带格式的: 下标

带格式的: 字体: (中文) 宋体, (中文) 中文(中国)

带格式的: 下标

带格式的: 下标



448
 449 **Figure 6.** An integrated diagram for the reactions and meltings of CaCO_3 and MgCO_3 in the
 450 Earth's deep mantle. Besides the reaction lines of R2-R4, two solidi of carbonate systems
 451 ($\text{CaCO}_3\text{-MgCO}_3$ marked as Ca-Mg (Thomson et al., 2014) and $(\text{K,Na})_2\text{Ca}_4(\text{CO}_3)_5$ marked as Ca-
 452 K-Na (Litasov et al., 2013)) are included here for discussions.

453
 454

455 4 Conclusions

456 In this study, we have calculated the thermodynamic properties of CaCO_3 with extensive
 457 first principles simulations over wide range of temperatures and pressures. The re-scaling
 458 method we proposed to eliminate the systematic errors in the simulated results shows its success
 459 in predicting various properties that are in good agreement with experiments and facilitates the
 460 precise comparisons among different datasets. The combination of lattice dynamics and
 461 molecular dynamics simulations provides a simple way to calculate the free energy with
 462 anharmonicity and increases the accuracy of calculated properties at high temperatures.

463 Based on these methods, we derive the phase diagram of CaCO_3 that is in accord with
 464 most recent experiments and suggest that kinetic effects may influence the experimental
 465 determined phase transitions. The phase boundaries of sp^3 bonding tetrahedrally structured high
 466 pressure polymorphs (the " $\text{CaCO}_3\text{-}P2_1/c\text{-h}$ " phase and the "pyroxene-type" phase) are found to
 467 be sensitive to temperature. These results clarify the strong temperature effects that have not
 468 been systematically explored before and provide new constraints on the stability of CaCO_3 under
 469 deep mantle conditions.

470 Finally, we find that high temperature greatly increases the tendency of partitioning
471 calcium of CaCO_3 into the silicates and produce CaSiO_3 . From both the reactions with MgSiO_3
472 and SiO_2 , CaCO_3 turns out to be less stable relative to the other forms of carbon (MgCO_3 , CO_2 or
473 C) over mantle conditions. Different from the findings of previous theoretical predictions,
474 CaCO_3 cannot be re-stabilized even in the cold slabs and thus is not the major host of carbon in
475 the Earth's deep mantle.

476

477

478 **Acknowledgments**

479 We acknowledge support from the Strategic Priority Research Program (B) of Chinese
480 Academy of Sciences (#XDB18000000). Z. Zhang acknowledges the supports from National
481 Natural Science Foundation of China (41474156, 41020134003). All the simulations were
482 carried out on the computational facilities in the Computer Simulation Lab of IGGCAS.

483

484

485 **References**

486 Biellmann, C., Gillet, P., Guyot, F., Peyronneau, J., Reynard, B. (1993). Experimental-evidence
487 for carbonate stability in the Earths lower mantle. *Earth and Planetary Science Letters*, 118, 31-
488 41.

489 Brenker, F.E., Vollmer, C., Vincze, L., Vekemans, B., Szymanski, A., Janssens, K., Szaloki, I.,
490 Nasdala, L., Joswig, W., Kaminsky, F. (2007). Carbonates from the lower part of transition zone
491 or even the lower mantle. *Earth and Planetary Science Letters*, 260, 1-9.

492 Fei, Y.W., Ricolleau, A., Frank, M., Mibe, K., Shen, G.Y., Prakapenka, V. (2007). Toward an
493 internally consistent pressure scale. *Proceedings of the National Academy of Sciences of the*
494 *United States of America*, 104, 9182-9186.

495 [Fiquet, G., Reynard, B. \(1999\). High-pressure equation of state of magnesite: New data and a](#)
496 [reappraisal. *American Mineralogist*, 84, 856-860.](#)

497 Gavryushkin, P. N., Martirosyan, N. S., Inerbaev, T. M., Popov, Z. I., Rashchenko, S. V.,
498 Likhacheva, A. Y., Lobanov, S. S., Goncharov, A. F., Prakapenka, V. B., and Litasov, K. D.
499 (2017). Aragonite-II and CaCO_3 -VII: New high-pressure, high-temperature polymorphs of
500 CaCO_3 , *Crystal Growth & Design*, 17(12), 6291-6296.

501 Hammouda, T., Laporte, D. (2000). Ultrafast mantle impregnation by carbonatite melts.
502 *Geology*, 28, 283-285.

503 Hammouda, T., Keshav, S. (2015). Melting in the mantle in the presence of carbon: Review of
504 experiments and discussion on the origin of carbonatites. *Chemical Geology*, 418, 171-188.

505 Holland, T.J., Hudson, N.F., Powell, R., Harte, B. (2013). New thermodynamic models and
506 calculated phase equilibria in NCFMAS for basic and ultrabasic compositions through the
507 transition zone into the uppermost lower mantle. *Journal of Petrology*, 54, 1901-1920.

508 Huang, W.-L., Wyllie, P.J. (1976). Melting relationships in the systems CaO-CO_2 and MgO-CO_2
509 to 33 kilobars. *Geochimica et Cosmochimica Acta*, 40, 129-132.

带格式的: 字体: 倾斜

510 Irving, A.J., Wyllie, P.J. (1973). Melting relationships in CaO-CO₂ and MgO-CO₂ to 36 kilobars
511 with comments on CO₂ in the mantle. *Earth and Planetary Science Letters*, 20, 220-225.

512 Kakizawa, S., Inoue, T., Suenami, H., Kikegawa, T. (2015). Decarbonation and melting in
513 MgCO₃-SiO₂ system at high temperature and high pressure. *Journal of Mineralogical and*
514 *Petrological Sciences*, 110(4): 179-188.

515 Kaminsky, F. (2012). Mineralogy of the lower mantle: A review of 'super-deep' mineral
516 inclusions in diamond. *Earth-Science Reviews*, 110(1-4), 127-147.

517 Keppler, H., Wiedenbeck, M., Shcheka, S.S. (2003). Carbon solubility in olivine and the mode of
518 carbon storage in the Earth's mantle. *Nature*, 424, 414-416.

519 Kresse, G., Joubert, D. (1999). From ultrasoft pseudopotentials to the projector augmented-wave
520 method. *Physical Review B*, 59, 1758-1775.

521 Li, Y., Zou, Y.T., Chen, T., Wang, X.B., Qi, X.T., Chen, H.Y., Du, J.G., Li, B.S. (2015). P-V-T
522 equation of state and high-pressure behavior of CaCO₃ aragonite. *American Mineralogist*, 100,
523 2323-2329.

524 Li, X., Zhang, Z., Lin, J.-F., Ni, H., Prakapenka, V.B., Mao, Z. (2018). New high pressure phase
525 of CaCO₃ at the topmost lower mantle: Implication for the deep mantle carbon transportation.
526 *Geophysical Research Letters*, doi: 10.1002/2017GL076536.

527 Li, Z.Y., Li, J., Lange, R., Liu, J.C., Mintzer, B. (2017). Determination of calcium carbonate and
528 sodium carbonate melting curves up to Earth's transition zone pressures with implications for the
529 deep carbon cycle. *Earth and Planetary Science Letters*, 457, 395-402.

530 Litasov, K.D., Goncharov, A.F., Hemley, R.J. (2011a). Crossover from melting to dissociation of
531 CO₂ under pressure: Implications for the lower mantle. *Earth and Planetary Science Letters*,
532 309, 318-323.

533 Litasov, K.D. (2011b). Physicochemical conditions for melting in the Earth's mantle containing a
534 C-O-H fluid (from experimental data). *Russian Geology and Geophysics*, 52 (5), 475-492.

535 Litasov, K.D., Shatskiy, A., Ohtani, E., Yaxley, G.M. (2013). Solidus of alkaline carbonatite in
536 the deep mantle. *Geology*, 41, 79-82.

537 Litasov, K.D., Shatskiy, A., Gavryushkin, P.N., Bekhtenova, A.E., Dorogokupets, P.I., Danilov,
538 B.S., Higo, Y., Akilbekov, A.T., Inerbaev, T.M. (2017). P-V-T equation of state of CaCO₃
539 aragonite to 29 GPa and 1673 K: In situ X-ray diffraction study. *Physics of the Earth and*
540 *Planetary Interiors*, 265, 82-91.

541 Lobanov, S.S., Dong, X., Martirosyan, N.S., Samtsevich, A.I., Stevanovic, V., Gavryushkin,
542 P.N., Litasov, K.D., Greenberg, E., Prakapenka, V.B., Oganov, A.R., Goncharov, A.F. (2017).
543 Raman spectroscopy and x-ray diffraction of sp³ CaCO₃ at lower mantle pressures. *Physical*
544 *Review B*, 96, 104101.

545 Luth, R.W. (1999). Carbon and carbonates in the mantle, in: Fei, Y.W., Bertka, C.M., Mysen,
546 B.O. (Eds.), *Mantle Petrology: Field Observations and High Pressure Experimentation: A*
547 *Tribute to Francis R. (Joe) Boyd*. Geochemical Society.

548 Luth, R. W. (2014). Volatiles in Earth's Mantle, in *Treatise on Geochemistry* (Second Edition),
549 edited by H. D. H. K. Turekian, pp. 355-391, Elsevier, Oxford.

带格式的: 下标

带格式的: 下标

带格式的: 字体: 倾斜

带格式的: 下标

带格式的: 字体: 倾斜

带格式的: 缩进: 左侧: 0 厘米, 首行缩进: 0 厘米

带格式的: 字体: 倾斜

- 550 Maeda, F., Ohtani, E., Kamada, S., Sakamaki, T., Hirao, N., Ohishi, Y. (2017). Diamond
551 formation in the deep lower mantle: a high- pressure reaction of MgCO₃ and SiO₂. *Scientific*
552 *Reports*, 7, 40602.
- 553 Martinez, I., Zhang, J.Z., Reeder, R.J. (1996). In situ X-ray diffraction of aragonite and dolomite
554 at high pressure and high temperature: Evidence for dolomite breakdown to aragonite and
555 magnesite. *American Mineralogist*, 81, 611-624.
- 556 Merlini, M., Hanfland, M., Crichton, W.A. (2012). CaCO₃-III and CaCO₃-VI, high-pressure
557 polymorphs of calcite: Possible host structures for carbon in the Earth's mantle. *Earth and*
558 *Planetary Science Letters*, 333, 265-271.
- 559 Monserrat, B., Drummond, N.D., Needs, R.J. (2013). Anharmonic vibrational properties in
560 periodic systems: energy, electron-phonon coupling, and stress. *Physical Review B*, 87, 144302.
- 561 Oda, H., Anderson, O.L., Isaak, D.G., Suzuki, I. (1992). Measurement of elastic properties of
562 single-crystal CaO up to 1200-K. *Physics and Chemistry of Minerals*, 19, 96-105.
- 563 Oganov, A.R., Glass, C.W., Ono, S. (2006). High-pressure phases of CaCO₃: Crystal structure
564 prediction and experiment. *Earth and Planetary Science Letters*, 241, 95-103.
- 565 Oganov, A.R., Ono, S. (2004). Theoretical and experimental evidence for a post-perovskite
566 phase of MgSiO₃ in Earth's D" layer. *Nature*, 430, 445-448.
- 567 Oganov, A.R., Ono, S., Ma, Y.M., Glass, C.W., Garcia, A. (2008). Novel high-pressure
568 structures of MgCO₃, CaCO₃ and CO₂ and their role in Earth's lower mantle. *Earth and*
569 *Planetary Science Letters*, 273, 38-47.
- 570 Ono, S., Kikegawa, T., Ohishi, Y. (2007). High-pressure transition of CaCO₃. *American*
571 *Mineralogist*, 92, 1246-1249.
- 572 Ono, S., Kikegawa, T., Ohishi, Y., Tsuchiya, J. (2005). Post-aragonite phase transformation in
573 CaCO₃ at 40 GPa. *American Mineralogist*, 90, 667-671.
- 574 Pickard, C.J., Needs, R.J. (2015). Structures and stability of calcium and magnesium carbonates
575 at mantle pressures. *Physical Review B*, 91, 104101.
- 576 Rohrbach, A., Schmidt, M.W. (2011). Redox freezing and melting in the Earth's deep mantle
577 resulting from carbon-iron redox coupling. *Nature*, 472, 209-212.
- 578 Seto, Y., Hamane, D., Nagai, T. & Fujino, K. (2008). Fate of carbonates within oceanic plates
579 subducted to the lower mantle, and a possible mechanism of diamond formation. *Physics and*
580 *Chemistry of Minerals*, 35, 223-229 (2008)
- 581 Shatskiy, A.F., Litasov, K.D., Palyanov, Y.N. (2015). Phase relations in carbonate systems at
582 pressures and temperatures of lithospheric mantle: review of experimental data. *Russian Geology*
583 *and Geophysics*, 56, 113-142.
- 584 Spivak, A.V., Litvin, Y.A., Ovsyannikov, S.V., Dubrovinskaia, N.A., Dubrovinsky, L.S. (2012).
585 Stability and breakdown of (CaCO₃)-C¹³ melt associated with formation of C¹³-diamond in static
586 high pressure experiments up to 43 GPa and 3900 K. *Journal of Solid State Chemistry*, 191, 102-
587 106.
- 588 Stixrude, L., Lithgow-Bertelloni, C., Kiefer, B., Fumagalli, P. (2007). Phase stability and shear
589 softening in CaSiO₃ perovskite at high pressure. *Physical Review B*, 75, 024108.

带格式的: 字体: 倾斜

带格式的: 字体: 倾斜

带格式的: 字体: 倾斜

- 590 [Stixrude, L., Lithgow-Bertelloni, C. \(2012\). Geophysics of Chemical Heterogeneity in the](#)
591 [Mantle. *Annual Review of Earth and Planetary Sciences*, 40, 569-595.](#)
- 592 [Stixrude, L., Lithgow-Bertelloni, C. \(2011\). Thermodynamics of mantle minerals - II. Phase](#)
593 [equilibria. *Geophysical Journal International*, 184, 1180-1213.](#)
- 594 Suito, K., Namba, J., Horikawa, T., Taniguchi, Y., Sakurai, N., Kobayashi, M., Onodera, A.,
595 Shimomura, O., Kikegawa, T. (2001). Phase relations of CaCO₃ at high pressure and high
596 temperature. *American Mineralogist*, 86, 997-1002.
- 597 Thomson, A.R., Walter, M.J., Lord, O.T., Kohn, S.C. (2014). Experimental determination of
598 melting in the systems enstatite-magnesite and magnesite-calcite from 15 to 80 GPa. *American*
599 *Mineralogist*, 99, 1544-1554.
- 600 Thomson, A.R., Walter, M.J., Kohn, S.C., Brooker, R.A. (2016). Slab melting as a barrier to
601 deep carbon subduction. *Nature*, 529, 76-79.
- 602 Togo, A., Tanaka, I. (2015). First principles phonon calculations in materials science. *Scripta*
603 *Materialia*, 108, 1-5.
- 604 Walter, M.J., Kohn, S.C., Araujo, D., Bulanova, G.P., Smith, C.B., Gaillou, E., Wang, J., Steele,
605 A., Shirey, S.B. (2011). Deep mantle cycling of oceanic crust: evidence from diamonds and their
606 mineral inclusions. *Science*, 334, 54-57.
- 607 Zedgenizov, D.A., Ragozin, A.L., Kalinina, V.V., Kagi, H. (2016). The mineralogy of Ca-rich
608 inclusions in sublithospheric diamonds. *Geochemistry International*, 54, 890-900.
- 609 [Zhang, D.B., Sun, T., Wentzcovitch, R. \(2014\). Phonon quasiparticles and anharmonic free](#)
610 [energy in complex systems. *Physical Review Letters*, 112, 058501.](#)
- 611 Zhang, Z.G., Liu, Z.R. (2015). High pressure equation of state for molten CaCO₃ from first
612 principles simulations. *Chinese Journal of Geochemistry*, 34, 13-20.
- 613 Zhang, Z.G., Stixrude, L., Brodholt, J. (2013). Elastic properties of MgSiO₃-perovskite under
614 lower mantle conditions and the composition of the deep Earth. *Earth and Planetary Science*
615 *Letters*, 379, 1-12.
- 616
- 617

带格式的: 字体: 倾斜

带格式的: 字体: 倾斜